Progress In Electromagnetics Research C, Vol. 101, 105–118, 2020

Thermal Characteristics of Hybrid Excitation Double Stator Bearingless Switched Reluctance Motor

Qianwen Xiang, Liyun Feng*, Yanjun Yu, and Kunhua Chen

Abstract—In order to research the temperature distribution of a hybrid excitation double stator bearingless switched reluctance motor (HEDSBSRM), the finite element method (FEM) is used to conduct thermal modeling and analysis. First, 2D FEM is used to calculate the losses of the motor, including the core losses and copper losses of the windings. Then, in the thermal analysis module of ANSYS Workbench software, losses are used for calculation and analysis as the thermal load. Furthermore, in order to enhance the accuracy of modeling, this paper also considers the equivalent thermal conductivity of each part of the motor, and the equivalent insulation of the windings and surface convection heat transfer coefficient are also considered. Finally, the simulation results of motor temperature field distribution are analyzed and studied in detail. The thermal characteristic is also of guiding significance to the optimal design of the motor.

1. INTRODUCTION

Due to its advantages such as no mechanical wear, high critical speed, high efficiency, and high power density, bearingless switched reluctance motor (BSRM) has become one of the hot spots in the research field of novel bearingless motor [1–4]. BSRM combines the advantages of switched reluctance motor (SRM) and magnetic bearing. Therefore, BSRM has broad application prospects in flywheel energy storage, high-speed machine tools, aerospace, and other high-speed drive fields. In recent years, there are some popular directions in BSRMs, such as mathematical model, control strategy, decoupling problem, vibration noise, losses, and thermal analysis [5–8]. However, the effect of temperature rise on performance of BSRMs has not been widely studied.

The coupling problem between suspension force and torque is solved in the structure of a double stator bearingless switched reluctance motor (DSBSRM). The electromagnetic characteristic of the proposed HEDSBSRM in [9] is better than that of the traditional DSBSRM. HEDSBSRM further reduces the power consumption. However, owing to the presence of two sets of concentrated windings and permanent magnets (PMs) on the inner-stator, the temperature rise may cause insulation deterioration. It is possible that the performance and normal operation of the motor are affected by the safety hazard caused by long working hours. Besides, the effect caused by PM itself is very important for the performance of the motor. Thus, the temperature of all parts of the HEDSBSRM must be kept within the range of safe operation. Therefore, it is necessary to study the temperature characteristics of the motor in different environments. Although the study of electromagnetic field by finite element analysis has reached the practical application level, there are still few studies on the loss calculation and temperature analysis of BSRM [10]. In the study of temperature fields, ordinary motors are more common than bearingless motors. The thermal analyses of the bearingless permanent magnet motor and the ordinary permanent magnet motor are not different in the research method. The only difference is the establishment of the thermal model, that is, the research object is different [11–14]. Therefore,

Received 11 September 2019, Accepted 17 January 2020, Scheduled 20 April 2020
* Corresponding author: Liyun Feng (fly_95@163.com).
The authors are with the School of Electrical and Information Engineering, Jiangsu University, Zhenjiang 212013, China.

similarly, this paper refers to the related research of SRM to analyze the thermal characteristics of BSRM [15–20].

Section 2 briefly introduces the structure, magnetic density waveform of the special point, and differential equation for heat conduction. In Section 3, the core losses of the motor are analyzed and calculated by FEM. The distribution characteristics of core losses are expounded. Besides, the copper losses of windings are calculated by the relevant formulas. The magnetothermal unidirectional coupling method is used to establish the temperature model of HEDSBSRM, namely the 3D finite element analysis model in Section 4. Meanwhile, the basic assumptions and reasonable boundary conditions for the application environment are given. Thermal analysis is performed under natural cooling conditions. Then, the results are compared and analyzed in Section 5 to observe the temperature distribution of various parts of the motor. Research on temperature field in this paper also has reference values for stable operation of the motor.

2. BASIC THEORY OF THERMAL ANALYSIS

2.1. Topology and Principle Analysis of the Motor

The topology of the HEDSBSBM is shown in Fig. 1, whose power is 1.8 kw. It can be seen that the motor consists of a 24-pole outer-stator, a 16-pole rotor, and an 8-pole hybrid inner-stator. The outer-stator, rotor, and hybrid inner-stator are coaxially nested from outside to inside in order. Four PMs are symmetrically distributed in eight poles of inner-stator. The radial width of PM is equal to the width of inner-stator poles to prevent leakage of the PM. For the HEDSBSRM, the working principle of the torque is similar to the conventional SRMs which follow the "minimum principle of reluctance". The suspension force is generated by the interaction of the PMs on the inner-stator and suspension windings. The bias magnetic flux provided by the PMs cooperates with the magnetic flux provided by the suspension windings to increase the power of the motor. That is to say, hybrid excitation instead of electric excitation improves efficiency. Due to the small power of the motor, the motor is designed to be cooled by natural air. Specific parameters of the HEDSBSRM are shown in Table 1.

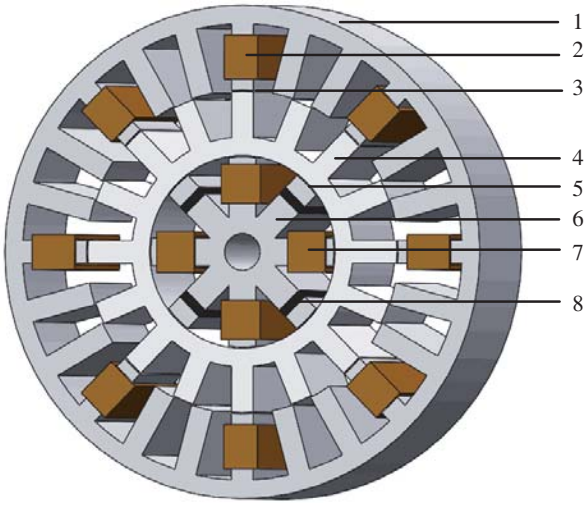

1-Outer stator; 2-Torque winding; 3-Air gap1; 4-Rotor;
5-Air gap2; 6-Inner stator; 7-Suspension winding; 8-PM

Figure 1. Topology of HEDSBSRM.

2.2. Analysis of Magnetic Density

The magnetic field of the core is analyzed qualitatively by studying the change of the magnetic density waveform of the special point on the motor. Studying the distribution law of magnetic density provides

Table 1. Values of the major parameters.

Parameters	Value	Parameters	Value
Inner-stator Pole Area/mm^2	255	Rotor Yoke Thickness/mm	4.18
Outer-stator Outer Diameter/mm	113	Outer-stator Yoke Thickness/mm	4.2
Rotor Outer Diameter/mm	72	The rotor pole arc	8°
Outer-stator Inner Diameter/mm	72.3	Axial Length/mm	37.5
Inner-stator Width	6	PM Width/mm	2

evidence for subsequent analysis of the distribution of core losses. Since the magnetic density of each point is a varying space vector, its magnitude and direction vary with the rotor position. In order to analyze the magnetic density characteristics of different positions accurately, the stator and rotor are respectively divided into four regions, which are the tip, middle, root of the tooth pole, and yoke. Four typical points are selected in each area, and their distribution is as shown in Fig. 2.

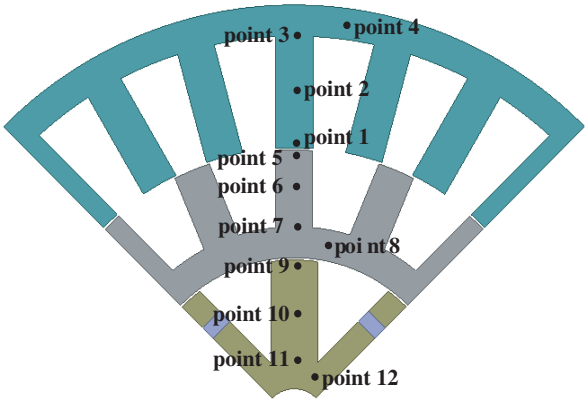

Figure 2. Distribution of typical points.

2.2.1. Magnetic Flux Analysis of Outer-Stator

The simulation results of the magnetic flux density waveform of various typical points in radial and tangential subspaces on the outer-stator are shown in Fig. 3. The radial and tangential magnetic flux density of typical points are recorded as B_r and B_t, respectively. As can be seen from the figure, the magnetic flux density of typical points is periodically variable. Each rotation of the rotor by 22.5° corresponds to a periodic change of magnetic flux density.

In Fig. 3(a), point 1 shows radial and tangential magnetic flux densities. In addition, B_r is greater than B_t, and both of them fluctuate up and down. In Fig. 3(b), B_t at point 2 is almost equal to zero which can be regarded as containing only B_r. This is because the magnetic path through the point 2 on the outer-stator is radial. At the same time, the waveform of B_r approximates sinusoidal waveform. In Fig. 3(c), B_t at point 3 does not change with angle and remains constant at about 0.12 T. B_r fluctuates up and down around 0.2 T. In Fig. 3(d), it can be seen that B_r of point 4 remains unchanged at approximately 0.14 T, and B_t fluctuates up and down around 0.25 T.

2.2.2. Magnetic Flux Analysis of Rotor

In Fig. 4, the magnetic flux density waveform of various typical points on the rotor can be seen in detail. In Fig. 4(a), on the whole, B_r at point 1 is greater than B_t, and both of them fluctuate up and down. Moreover, as can be seen from Fig. 4(b), B_t at point 6 is almost equal to zero. B_r is similar in size to point 5. In Fig. 4(c), point 7 shows B_r and B_t. The values of them are not much different, about

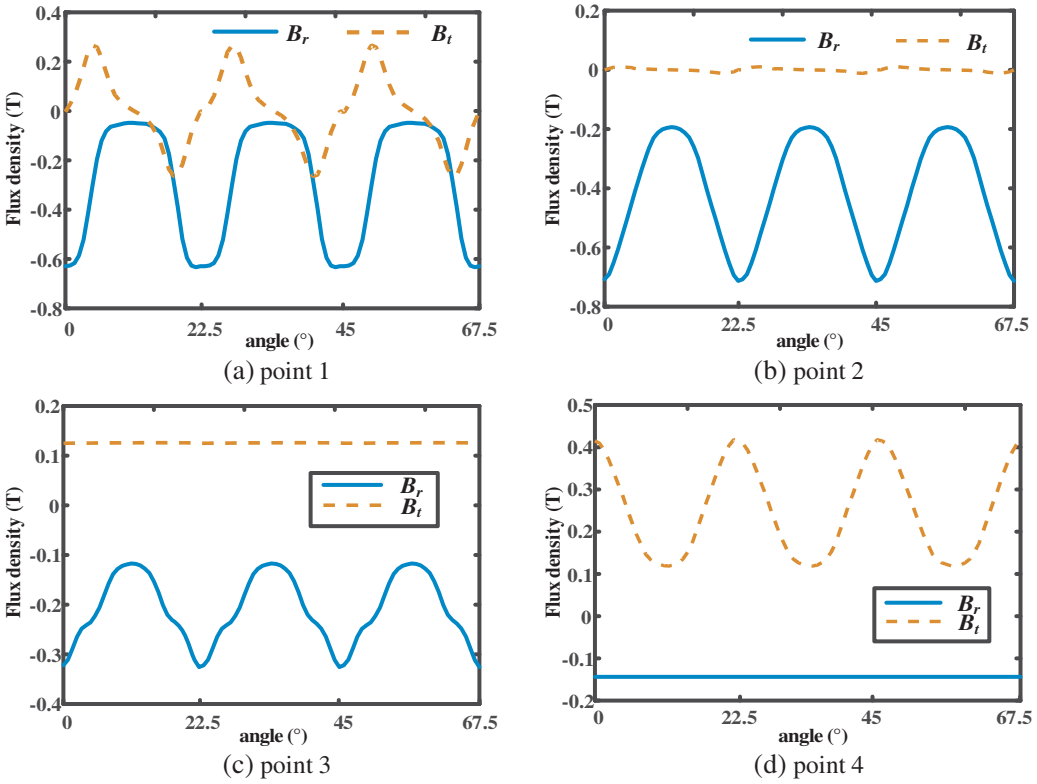

Figure 3. Magnetic density waveform on the outer-stator.

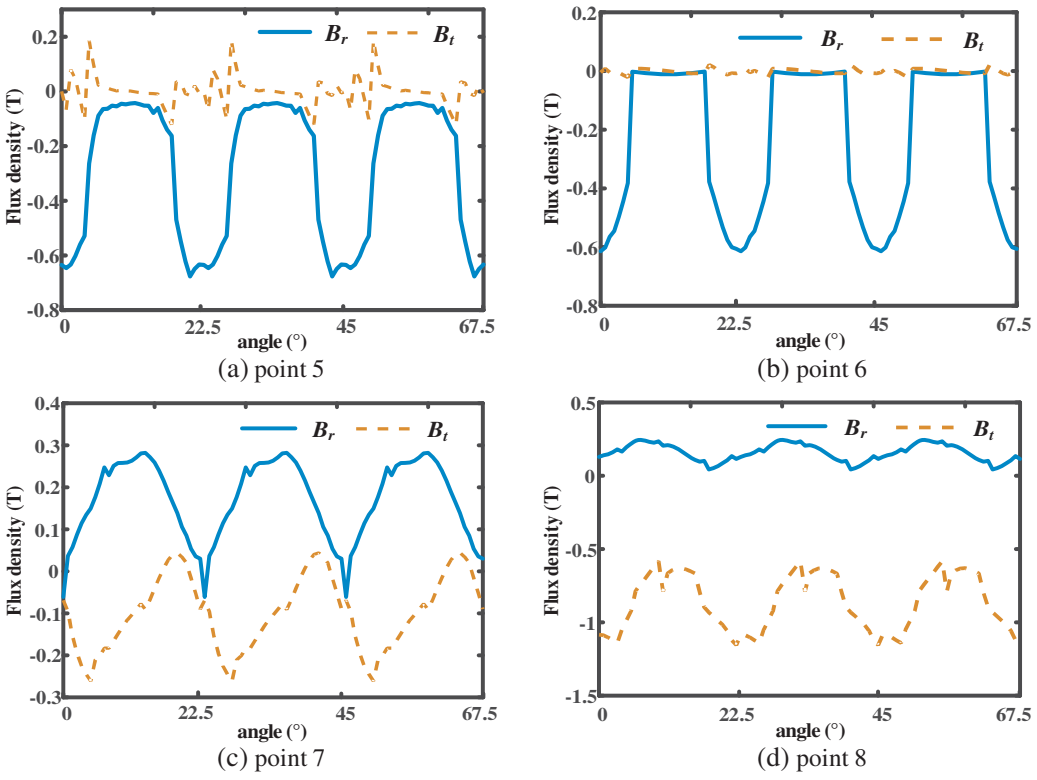

Figure 4. Magnetic density waveform on the rotor.

0.28 T. Relatively, B_r is smaller at point 8 in Fig. 4(d), about 0.1 T. The value of B_t is between 0.6 T and 1.1 T.

2.2.3. Magnetic Flux Analysis of Inner-Stator

As shown in Fig. 5, both B_r and B_t do not change with angle in inner-stator. In Figs. 5(a) and (b), B_t at points 9 and 10 can be ignored. B_r of points 9 and 10 are almost 0.8 T and 1 T, respectively. Fig. 5(c) shows that B_r and B_t are close to 0.58 T and 0.12 T, respectively. Simultaneously, B_r and B_t are about 0.15 T and 0.72 T in Fig. 5(d).

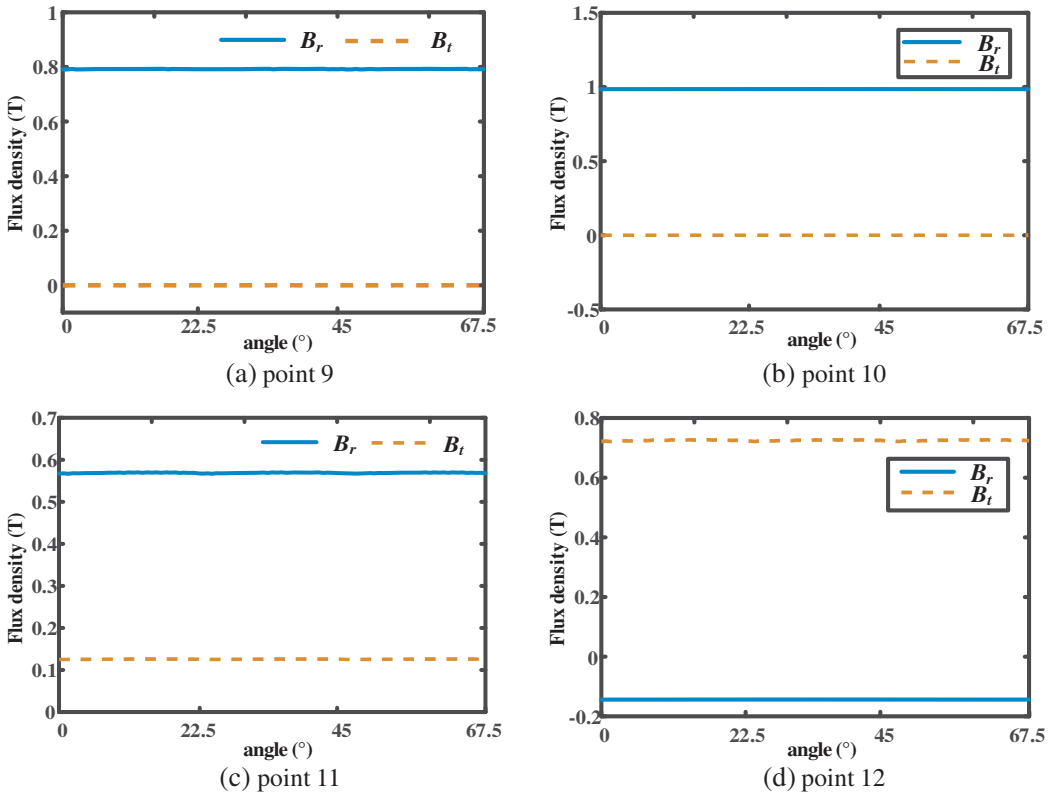

Figure 5. Magnetic flux density waveform on the inner-stator.

In conclusion, B_r of the yoke is generally smaller than other parts. However, B_t of the yoke is greater than other parts. For the center of the pole on the stator and rotor, the tangential magnetic flux density is basically equal to zero. The high nonlinearity of the magnetic field causes the difference in magnetic flux density of the various parts of the motor.

2.3. Differential Equation for Heat Conduction

The three basic modes of heat transfer are conduction, convection, and radiation, respectively. The formula of temperature rise analysis of HEDSBSRM is based on the differential equation of heat conduction, which is given as

$$k\nabla^2 T + Q = \rho c \frac{\partial T}{\partial \tau} \tag{1}$$

where k is the thermal conductivity; Q is the internal heat generation rate; ρ and c represent the material density of the motor and heat capacity, respectively.

Under rated operating conditions, HEDSBSRM can be regarded as a steady state field, which means that the temperature does not change with time. In order to describe the 3-D heat conduction

of the HEDSBSRM, formula (1) can be simplified to

$$k_x \frac{\partial^2 T}{\partial x^2} + k_y \frac{\partial^2 T}{\partial y^2} + k_z \frac{\partial^2 T}{\partial z^2} + Q = 0 \tag{2}$$

where k_x, k_y, and k_z are the thermal conductivities in the coordinate axial directions, respectively.

For convection heat exchange on the motor surface, the convection boundary condition is expressed as

$$-k \left. \frac{\partial T}{\partial n} \right|_a = h \left(T_a - T_x \right) \tag{3}$$

where h is the convective heat transfer coefficient, and T_a and T_x represent the temperatures of motor surface and environment, respectively.

3. LOSSES ANALYSIS

Losses are the main reason of temperature rise, caused by heat generated inside the motor. In this paper, core losses of stator and rotor and copper losses of two sets of windings are mainly considered as heat sources. Meanwhile, eddy current losses of PMs, stray, and mechanical losses are ignored.

3.1. Core Losses of Stator and Rotor

There are three main analytical methods for core loss calculation: experimental method, magnetic analysis method, and FEM. Comparatively speaking, this paper chooses to use FEM to carry out analytical calculation of core losses, which is more rapid and accurate. Through the finite element software ANSOFT, density distribution and numerical diagram of the core losses can be calculated. Dual-frequency method is used for ANSOFT finite element analysis. The essence of the dual-frequency method is to separate the hysteresis losses and eddy current losses according to the magnetic field simulation results. The eddy current losses and hysteresis losses are analyzed by fast Fourier analysis and the maximum magnetic density value. The maximum magnetic density method ignores the influence of the position of the local hysteresis loop on the losses. The hysteresis losses are only related to the amplitude of the main hysteresis loop and local hysteresis loop. Density distributions of core losses of motor at different rotor positions θ are shown in Figs. 6 and 7. As can be seen from the figure, due to the different distributions of magnetic field lines at different positions, the distributions of core losses densities are also different. Obviously, the core loss of rotor and outer-stator is greater than that of inner-stator. This is because both the torque magnetic field and suspension magnetic field pass through the rotor, and the rotation of the rotor causes the magnetic field to change rapidly. In addition, for the outer-stator, core losses of the tooth are greater than that of the yoke. For the rotor, the distribution of core losses of the tooth is more uniform than that of the yoke. For the inner-stator, the core losses

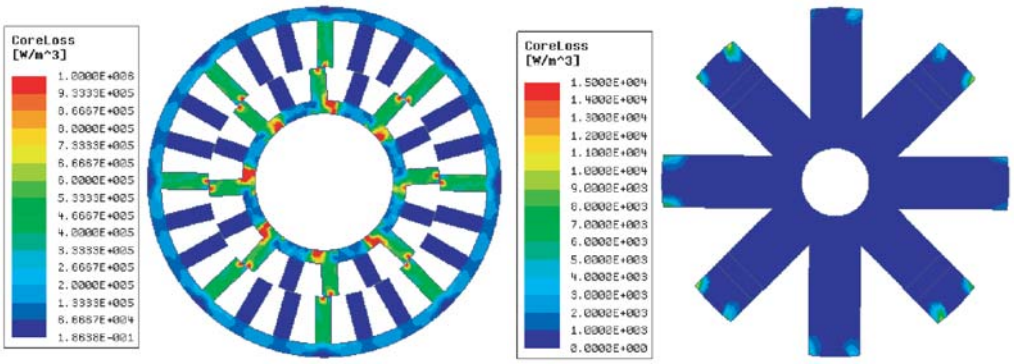

(a) outer-statorand rotor (b) inner-stator

Figure 6. Distribution of core loss density when $\theta = 3.75°$.

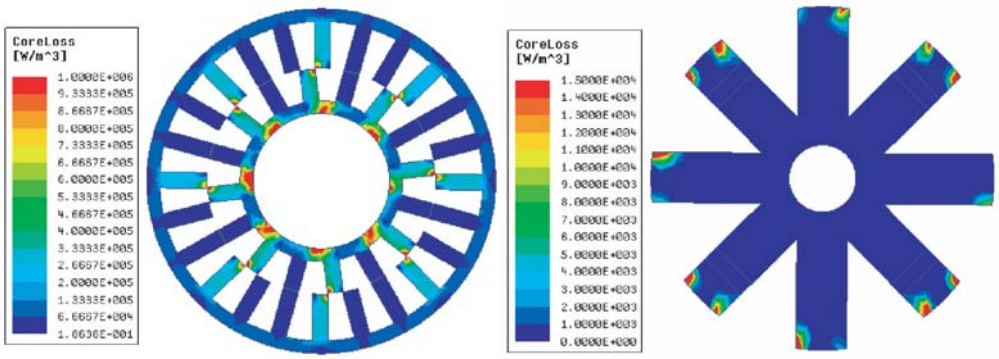

(a) outer-statorand rotor (b) inner-stator

Figure 7. Distribution of core losses density when $\theta = 7.5°$.

are concentrated on the tooth. When $\theta = 7.5°$, core losses of the outer-stator and rotor are less than $\theta = 3.75°$ while core losses of the inner-stator are larger than $\theta = 3.75°$.

In Fig. 8, it can be seen that the core losses vary with θ. In summary, the core losses of rotor and outer-stator are greater than that of inner-stator. In Fig. 8(a), as the rotor yoke thickness increases, the core losses of outer-stator and rotor increase linearly first and then fluctuate up and down. There is little difference between the core losses of the outer-stator and rotor. In Fig. 8(b), the core losses of inner-stator fluctuate evenly up and down within the range of 0° to 7.5°. Within the range of 0° to 7.5°, the average core losses of outer-stator, rotor, and inner-stator are 14.35 W, 14.7 W, and 15.21 mW, respectively.

Figures 7 and 8 show that core losses of the inner-stator are significantly smaller than that of the rotor and outer-stator. The reason is that the magnetic field on the inner-stator does not change when the suspension is stable.

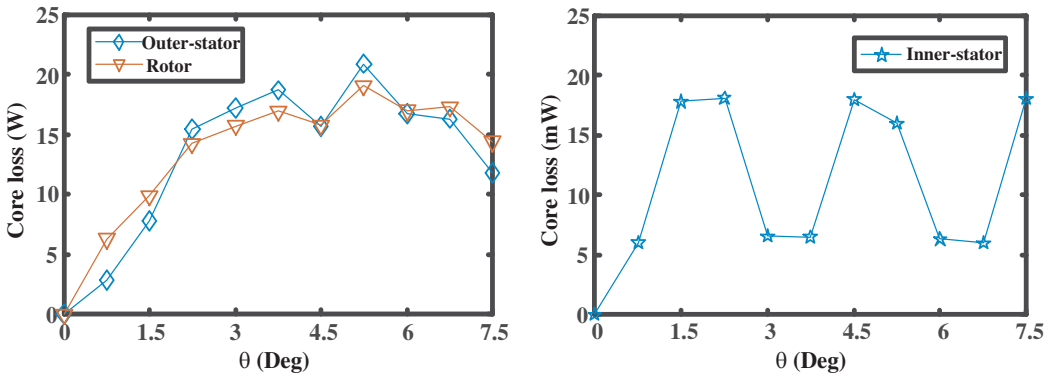

(a) outer-stator and rotor (b) inner-stator

Figure 8. Core loss.

3.2. Copper Losses of Windings

Copper losses are one of the main heat sources of the motor, which lead to higher winding temperature rise. When HEDSBSRM runs stably, according to Joule theorem, the copper losses of two sets of windings are proportional to the square of the effective current, which can be calculated by Eq. (4)

$$P_{cu} = m \cdot I_{rms}^2 \cdot R_{phase} \tag{4}$$

where m is the number of phases of the motor, equal to 3; I_{rms} is the effective value of the winding current; R_{phase} represents the resistance of the winding in one phase. The formula for calculating

resistance is

$$R_{phase} = \frac{\rho_c \cdot l}{s} \tag{5}$$

where ρ_c represents the resistivity of copper wire, and l and s are the length and sectional area of copper wire, respectively.

4. THERMAL MODELING OF THE HEDSBSRM

4.1. Internal Heat Generation Rate

The heat source in the HEDSBSRM comes from the loss in stable operation. The core losses and copper losses obtained in the previous chapter are coupled to the thermal analysis model respectively. In other words, the temperature field is analyzed by transforming the losses into internal heat generation rate. The heat generation rate of stator and rotor is calculated as

$$Q = \frac{P_{loss}}{V} \tag{6}$$

where Q is the internal heat generation rate, P_{loss} the copper loss or core loss, and V the volume of different parts of the motor.

In regard to the windings, internal heat generation rate is obtained as

$$Q = \rho_c \cdot J^2 \tag{7}$$

where J is the current density of copper wire.

The calculation result of the core losses is directly coupled to the thermal model for thermal analysis to obtain the temperature field distribution map of the motor. In addition, the internal heat generation rate of windings obtained from the above formulas and losses are listed in Table 2 below.

Table 2. Calculated internal heat generation rate.

Operation condition	Value
Copper losses of suspension windings (W/m^3)	300900
Copper losses of torque windings (W/m^3)	209393

4.2. Thermal Conductivity Coefficients

4.2.1. Equivalent Insulation

Owing to the complex winding structure, in order to simplify the model, the following assumptions are made: (a) neglecting the thermal resistance of the conductor; (b) no air gap between the insulating layers and the dipping lacquer is fully filled; (c) the insulated lacquer of copper wire is evenly distributed. According to the above hypothesis, the winding is treated as the equivalent part in the analysis of temperature field. Copper wire is equivalent to copper block. The groove insulation, dipping lacquer, and air in groove are regarded as an insulator, which is called equivalent insulation. The equivalent models of the torque and suspension windings are shown in Figs. 9 and 10.

The thermal conductivity of equivalent insulation λ_{eq} is calculated as [21]:

$$\begin{aligned}\lambda_{eq} \;=\; & 0.165(1 + 0.0007T_p) \times [1 - 0.32d(1 - 9.2k + 5.2k^2) + 0.81d^2] \\ & \times (2.1k_1^{1.5} - 0.32) \times (\lambda/0.162)^{1/3} \times (\lambda_a/0.143)^{0.25}\end{aligned} \tag{8}$$

where λ_{eq} and T_p are the core coefficient and average temperature of wire; d is the diameter of enameled wire; k represents the coefficient of invasion; and k_1 is the filling factor. The thermal conductivity of the dipping lacquer λ is 0.18, and that of the round copper wire insulation λ_a is 0.15.

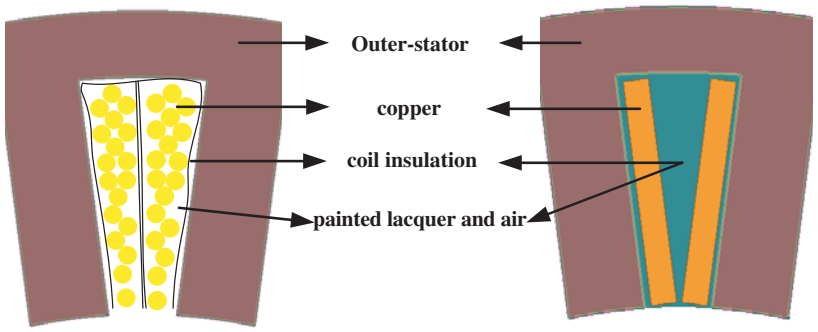

(a) Before equivalent treatments (b) After equivalent treatments

Figure 9. Equivalent treatment of torque windings.

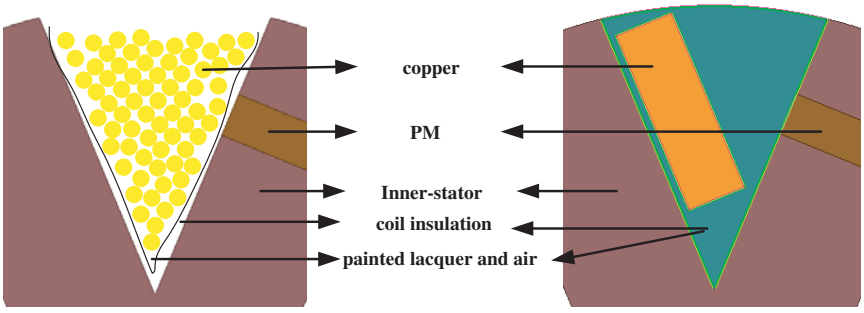

(a) Before equivalent treatments (b) After equivalent treatments

Figure 10. Equivalent treatment of suspension windings.

4.2.2. Equivalent Thermal Conductivity of Air Gap

As the rotor rotates, the air gap between the stator and rotor transfers heat by convection. If conventional boundary conditions are used between the stator and rotor, there will be some deviation. In addition, the thermal conductivity of the air gap is related to the flow velocity, specific heat, density, and other factors of the fluid, which is complex and difficult to calculate quantitatively. Therefore, in order to simplify the modeling, the equivalent thermal conductivity is introduced to treat the flowing air as static state. According to the empirical formula, the equivalent thermal conductivity coefficient λ_{eff1} of circumferential air gap between rotor and inner-stator can be obtained as

$$\lambda_{eff1} = 0.23\beta \left(\frac{\delta}{R_{ir}}\right)^{0.25} \left(\frac{v_{ir}}{v_0}\right)^{\frac{1}{2}} \cdot \lambda_k \tag{9}$$

where β is experience factor considering surface roughness of rotor, δ the air gap length, R_{ir} the rotor outer diameter, v_{ir} the linear velocity of inner circumference, v_o the kinematic viscosity of media in the air gap, and λ_k the thermal conductivity of media in the air gap.

For the HEDSBSRM, the air gap between the outer-stator and rotor is non-circumferential. However, the equivalent thermal conductivity coefficient λ_{eff2} is calculated based on the circumference due to the little coefficient difference, which can be expressed as

$$\lambda_{eff2} = 0.23\beta \left(\frac{\delta}{R_{or}}\right)^{0.25} \left(\frac{v_{or}}{v_0}\right)^{\frac{1}{2}} \cdot \lambda_k \tag{10}$$

where R_{or} represents the rotor outer diameter, and v_{or} represents linear velocity of outer circumference.

According to the empirical formula, the thermal conductivity coefficients in different parts of the HEDSBSRM are shown in Table 3.

Table 3. Thermal conductivity coefficients in different parts of the HEDSBSRM.

Parts	Materials	Thermal conductivity ($W/m \cdot k$)	Density (kg/m^3)	Specific heat capacity ($J/kg \cdot K$)
Stator and rotor	DW310-35	40/40/4.5	7650	460
Winding	Copper	401	8900	390
Equivalent insulation	Painted and insulated lacquer	0.26	1.2	1340
Shaft	Steel #45	43	7800	473
Air-gap	air	0.045	1.23	1003
Shell	Aluminum	200	2700	900

4.3. Convection Heat Transfer Coefficients in Surface

The fluid flowing through the surface can take away the heat of each part of the motor, which is the process of heat dissipation and surface cooling. Convection heat transfer between fluid and motor surface is of great significance to temperature research. Surface convective heat transfer coefficient is also known as heat dissipation coefficient, which depends on the fluid velocity, physical properties, specific heat capacity of materials, and other factors. Therefore, it is difficult to calculate accurately and quantitatively. In this paper, the surface heat dissipation coefficient mainly includes heat dissipation coefficient of the end-stator and end-windings, end-rotor and the frame.

4.3.1. Frame

The surface convective heat transfer coefficient of the motor in frame when it radiates heat to the surrounding medium is normally given as

$$\alpha_1 = 14\left(1 + \frac{\sqrt{w_0}}{2}\right)^3 \sqrt{\frac{T_0}{25}} \tag{11}$$

where α_1 is the surface heat dissipation coefficient, and ω_0 and T_o represent the speed of air blowing from the external surface and the ambient temperature. Because of the natural cooling chosen in this paper, α_1 can be written as

$$\alpha_1 = 14\sqrt{\frac{T_0}{25}} \tag{12}$$

where ω_0 is equal to 0 m/s.

4.3.2. End-stator and End-Windings

Most of the heat of the motor is dissipated through the motor casing. In addition to considering the heat dissipation coefficient of the radial surface, the axial direction is also essential. The end of the stator and the two sets of windings both have great influence on the axial temperature distribution of the motor. The simplified model is adopted in the windings. Thus, the convective heat transfer coefficient at the end-stator is considered equal to that of the end-windings, which can be defined as

$$\alpha_s = \alpha_w = \frac{1 + 0.04\nu_r}{0.045} \tag{13}$$

where v_r represents peripheral speed of the rotor, and α_s and α_w are the heat dissipation coefficient of end-stator and end-windings, respectively.

4.3.3. End-Rotor

In addition to the end-stator and end-windings, the axial surface heat dissipation coefficient also includes the end-rotor. In order to analyze the axial temperature distribution more accurately, the heat dissipation coefficient of the end-rotor surface can be obtained as:

$$\alpha_r = 28\,(1 + 0.45 v_r) \tag{14}$$

where α_r is the heat dissipation coefficient of end-rotor, and v_r is referred before.

Table 4 shows the specific values of the convection heat transfer coefficients in each surface of the HEDSBSRM.

Table 4. The convection heat transfer coefficients in each surface.

Operation condition	Value
α_f (W/m^2 · °C)	13.13
α_s (W/m^2 · °C)	45.68
α_m (W/m^2 · °C)	45.68
α_r (W/m^2 · °C)	124.49

4.4. Thermal Modeling by FEM

In order to obtain the temperature distribution of the HEDSBSRM, the 3-D motor model of HEDSBSRM is established by Maxwell software. The motor is imported into ANSYS Workbench module to establish thermal model, including equivalent insulation and equivalent air gap. As shown in Fig. 11, the thermal model includes frame, outer-stator, equivalent winding, PM, rotor, inner-stator, and shaft. Next, the material properties of the thermal model are added, which means that the thermal conductivity is set. And the grid is divided, as shown in Fig. 12. Then, the internal heat generation rate of windings and the surface convective heat dissipation coefficient are set on the components and surfaces of the motor. In addition, for core losses, they are directly unidirectionally coupled into the thermal model. Finally, the temperature field distribution is obtained by solving the model.

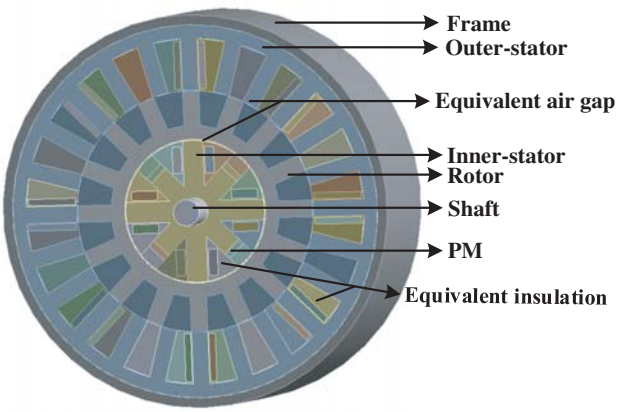

Figure 11. Thermal model of the HEDSBSRM.

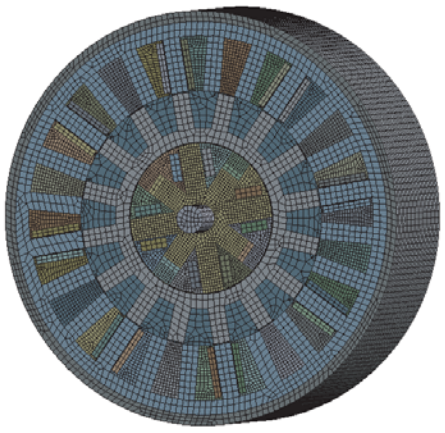

Figure 12. Thermal model of the HEDSBSRM.

5. SIMULATION RESULTS OF THE HEDSBSRM

According to the above, the co-simulation results of temperature field analysis of the HEDSBSRM are shown in Fig. 13. Obviously, due to the limited axial length of the motor, the overall temperature

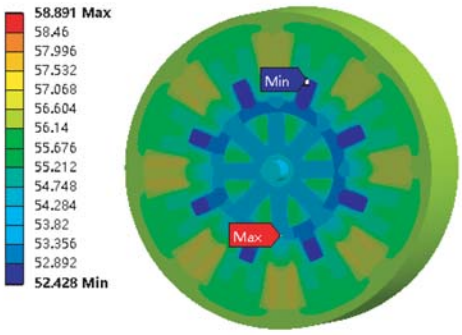

Figure 13. The thermal distribution of HEDSBSRM.

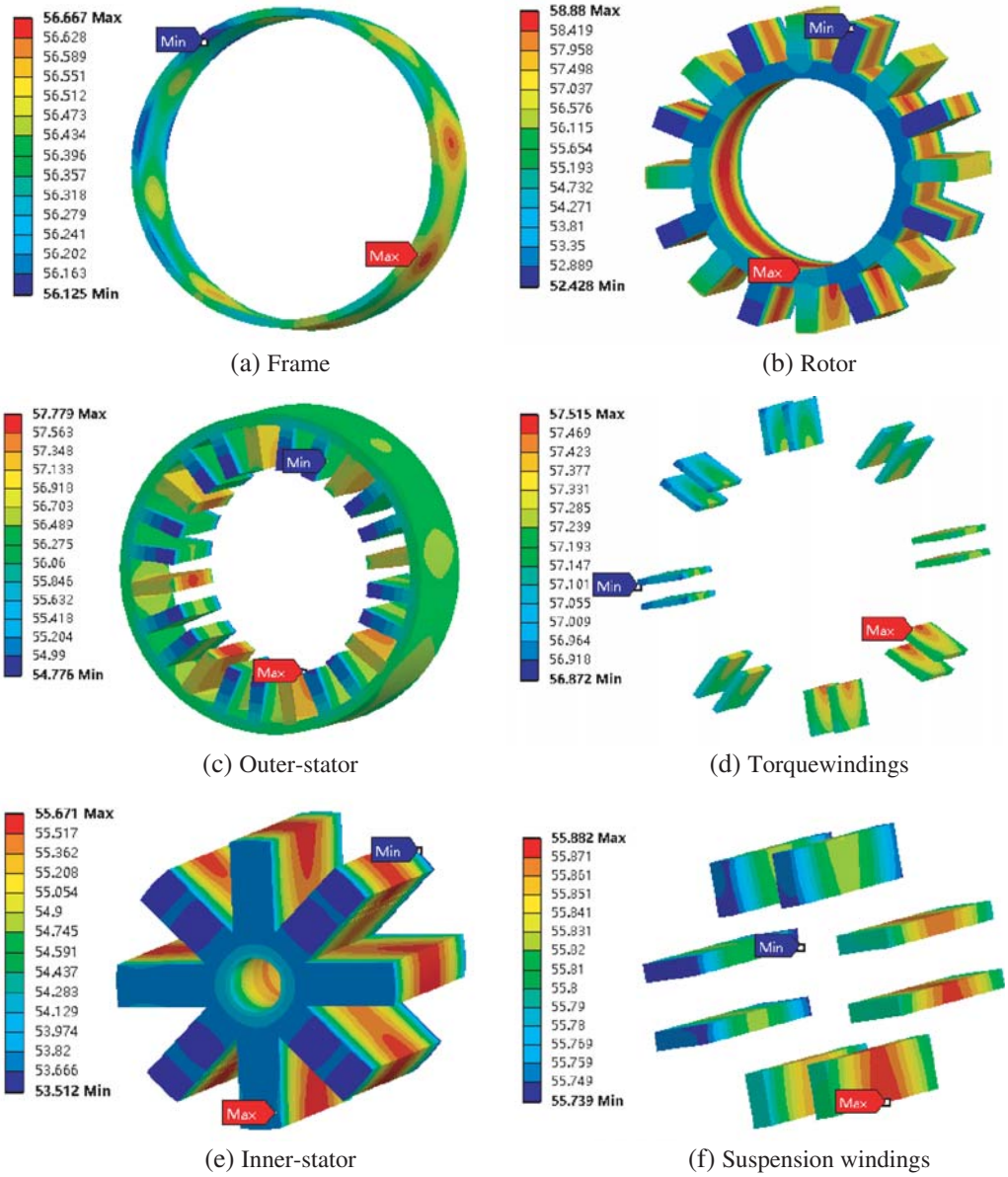

(a) Frame (b) Rotor

(c) Outer-stator (d) Torquewindings

(e) Inner-stator (f) Suspension windings

Figure 14. Temperature field distribution of the motor.

difference is not large. Furthermore, the highest and lowest temperatures both appear on the rotor, reaching 52.4°C and 58.9°C, respectively. The former is due to the absence of windings on the rotor, which means that the thermal conductivity of the equivalent air gap is less than the equivalent insulation. The latter is caused by the fast rate of change of magnetic field on the rotor. Therefore, the motor can operate safely and stably for a long time.

Figure 14 shows the specific temperature field distribution of each part of the motor. The highest temperature of the outer-stator and the highest temperature of torque windings are both up to more than 57.5°C. The maximum temperature of the inner-stator and suspension windings reaches about 55.6°C. In addition, the maximum temperatures of the frame and rotor are 56.7°C and 58.9°C, respectively. As can be observed from the figure, for the frame and two sets of windings, the difference in temperature is small, less than 1°C. For the inner-stator, outer-stator, and rotor, the temperature differences are approximately 2.1°C, 3°C, and 6.4°C, respectively. Due to the particularity of the structure of the motor, the highest temperature occurs at the rotor. The temperature of the rotor is generally higher than the stator. This is because the thermal conductivity of copper is significantly larger than that of silicon steel. Moreover, it is important that the temperature of the rotor and stator is up to the top value in the middle part and gradually decreases in the axial direction. The reason is that the thermal conductivity coefficient of equivalent insulators is low, and the internal heat cannot be dissipated. It can still be seen that the temperature of the toothed pole around the winding is higher than the yoke. In addition, the temperature of the rotor and outer-stator is generally higher than that of the inner-stator. This is because the magnetic field on the inner-stator is substantially unchanged.

6. CONCLUSION

In this paper, thermal modeling and characteristics of a hybrid excitation double stator bearingless switched reluctance motor are analyzed. In order to simulate the temperature field accurately, the core losses are unidirectionally coupled in the process of thermal modeling, and the copper losses are converted to the internal heat generation rate by calculation.

In summary, the simulation results prove that the motor can be guaranteed to operate reliably and safely for a long time under natural cooling. This paper has played a beneficial role in the reliable operation of detecting motor and winding and laid a good theoretical foundation for the optimal design and further experimental research of the HEDSBSRM.

ACKNOWLEDGMENT

This work was sponsored by the National Natural Science Foundation of China (51707082) Natural Science Foundation of Jiangsu Province (BK20170546 BK20150510) and Research Initiation Fund of Jiangsu University (14JDG075).

REFERENCES

1. Morrison, C. R., M. W. Siebert, and E. J. Ho, "Electromagnetic forces in a hybrid magnetic-bearing switched-reluctance motor," *IEEE Trans. Magn.*, Vol. 44, No. 12, 4626–4638, Dec. 2008.
2. Chen, L. and W. Hofmann, "Speed regulation technique of one bearingless 8/6 switched reluctance motor with simpler single winding structure," *IEEE Trans. Ind. Electron.*, Vol. 59, No. 6, 25922600, Feb. 2012.
3. Wei, P., D. Lee, and J. Ahn, "Design and analysis of double stator type bearingless switched reluctance motor," *Transactions of the Korean Institute of Electrical Engineers*, Vol. 60, No. 4, 746–752, 2011.
4. Xue, B., H. Wang, and J. Bao, "Design of novel 12/14 bearingless permanent biased switched reluctance motor," *International Conference on Electrical Machines and Systems. IEEE*, 2655–2660, Oct. 2014.

5. Cao, X., J. Zhou, C. Liu, and Z. Deng, "Advanced control method for single-winding bearingless switched reluctance motor to reduce torque ripple and radial displacement," *IEEE Trans. Energy Convers.*, Vol. 32, No. 4, 1533–1543, Dec. 2017.
6. Cao, X. and Z. Deng, "A full-period generating mode for bearingless switched reluctance generators," *IEEE Transactions on Applied Superconductivity*, Vol. 20, No. 3, 1072–1076, Mar. 2010.
7. Zhang, J., H. Wang, L. Chen, C. Tan, and Y. Wang, "Multi-objective optimal design of bearingless switched reluctance motor based on multi-objective genetic particle swarm optimizer," *IEEE Trans. Magn.*, Vol. 54, No. 1, 1–13, Oct. 2017.
8. Wang, H., J. Bao, B. Xue, and J. Liu, "Control of suspending force in novel permanent-magnet-biased bearingless switched reluctance motor," *IEEE Trans. Ind. Electron.*, Vol. 62, No. 7, 4298–4306, Jul. 2015.
9. Xiang, Q. W. and L. Feng, "Optimization and analysis of 24/16/8 hybrid excitation double stator bearingless switched reluctance motor," *Progress In Electromagnetics Research C*, Vol. 89, 191–205, 2019.
10. Liu, J., X. Zhang, H. Wang, and J. Bao, "Iron loss characteristic for the novel bearingless switched reluctance motor," *2013 International Conference on Electrical Machines and Systems (ICEMS)*, 586–592, Oct. 2013.
11. Su, B., X. Sun, L. Chen, Z. Yang, and K. Li, "Thermal modeling and analysis of bearingless permanent magnet synchronous motors," *International Journal of Applied Electromagnetics and Mechanics*, Vol. 56, No. 1, 115–130, 2017.
12. Kral, C., A. Haumer, and S. B. Lee, "A Practical thermal model for the estimation of permanent magnet and stator winding temperatures," *IEEE Trans. Power Electron.*, Vol. 29, No. 1, 455–464, Jul. 2013.
13. Fang, L., G. Tan, S. Yin, and K. Hu, "Design and temperature field analysis of a novel structure line-start permanent magnetsynchronous motor," *International Journal of Applied Electromagnetics and Mechanics*, Vol. 51, No. 3, 1–12, Feb. 2016.
14. Kefalas, D. T. and A. Kladas, "Thermal investigation of permanent-magnet synchronous motor for aerospace applications," *IEEE Trans. Ind. Electron.*, Vol. 61, No. 8, 4404–4011, Aug. 2014.
15. Arbab, N., W. Wang, C. Lin, J. Hearron, and B. Fahimi, "Thermal modeling and analysis of a double-stator switched reluctance motor," *IEEE Trans. Energy Convers.*, Vol. 30, No. 3, 1209–1217, Sept. 2015.
16. Pan, J., F. Meng, and N. Cheung, "Core loss analysis for the planar switched reluctance motor," *IEEE Trans. Magn.*, Vol. 50, No. 2, 813–816, Feb. 2014.
17. Sun, X., Z. Xue, X. Xu, and L. Chen, "Thermal analysis of a segmented rotor switched reluctance motor used as the belt-driven starter/generator for hybrid electric vehicles," *Journal of Low Power Electronics*, Vol. 12, No. 3, 277–284, Sept. 2016.
18. Chen, H., Y. Xu, and H. Iu, "Analysis of temperature distribution in power converter for switched reluctance motor drive," *IEEE Trans. Magn.*, Vol. 48, No. 2, 991994, Feb. 2012
19. Toda, H., K. Senda, S. Morimoto, and T. Hiratani, "Influence of various non-oriented electrical steels on motor efficiency and iron loss in switched reluctance motor," *IEEE Trans. Magn.*, Vol. 49, No. 7, 3850–3853, Jul. 2013.
20. Garcia-Amoros, J., P. Andrada, B. Blanque, and M. Marin-Genesca, "Influence of design parameters in the optimization of linear switched reluctance motor under thermal constraints," *IEEE Trans. Ind. Electron.*, Vol. 65, No. 2, 1875–1883, Feb. 2018.
21. Li, Y., "Research on loss and thermal analysis of switched reluctance motor," Nanjing University of Aeronautics and Astronautics, Nanjing, 2006.